

Supporting Information: Strongly Cavity-Enhanced Spontaneous Emission from Silicon-Vacancy Centers in Diamond

*Jingyuan Linda Zhang^{1‡}, Shuo Sun^{1‡}, Michael J. Burek^{2‡}, Constantin Dory¹, Yan-Kai Tzeng⁵,
Kevin A. Fischer¹, Yousif Kelaita¹, Konstantinos G. Lagoudakis¹, Marina Radulaski¹, Zhi-Xun
Shen^{3,4,5}, Nicholas A. Melosh^{3,4}, Steven Chu^{5,6}, Marko Lončar², Jelena Vučković¹*

¹E. L. Ginzton Laboratory, Stanford University, Stanford, California 94305, USA

²School of Engineering and Applied Sciences, Harvard University, Cambridge, Massachusetts
02138, USA

³Geballe Laboratory for Advanced Materials, Stanford University, Stanford, California 94305,
United States

⁴Stanford Institute for Materials and Energy Sciences, SLAC National Accelerator Laboratory,
Menlo Park, California 94025, USA

⁵Department of Physics, Stanford University, Stanford, California 94305, USA

⁶Department of Molecular and Cellular Physiology, Stanford University, Stanford, California
94305, USA

Material Synthesis and Device Fabrication

Fabrication of emitter-cavity systems began with a single-crystal diamond plate (Type IIa, < 1 ppm [N], Element Six), on which a nominally 100-nm-thick layer of diamond containing SiV^- centers was grown homoepitaxially via microwave plasma chemical vapor deposition (MPCVD).¹ The following growth conditions were used: H_2 : 300 sccm, CH_4 : 0.5 sccm, stage temperature 650 °C, microwave power 1.3 kW, and pressure: 23 Torr. The same growth condition has resulted in a SiV^- density of $3 \times 10^{14} \text{ cm}^{-3}$ on a different sample.²

Nanophotonic cavities are fabricated using electron beam lithography (EBL) followed by angled-etching.³⁻⁶ First, the etch mask pattern is defined in the electron beam resist Hydrogen silsesquioxane (HSQ) on the diamond substrate using EBL. The pattern is then transferred into the diamond substrate during a standard top-down anisotropic reactive ion etch step. Next, during the angled-etching, the anisotropic oxygen plasma etching is directed at an oblique angle with respect to the substrate, which releases the diamond nanobeams with triangular cross-sections. Lastly, the etch mask is removed in hydrofluoric acid, leaving free-standing diamond nanobeams.

The nanobeam photonic crystal cavity parameters were chosen to target a fundamental cavity mode near the silicon vacancy (SiV^-) center ZPL emission at $\lambda \sim 737 \text{ nm}$. The etch angle (θ), width (w), lattice constant (a) and minor (longitudinal) elliptical air hole diameters (d_x) are 50°, 468 nm, 257 nm, 141 nm, respectively. The major (transverse) elliptical air hole diameter (d_z) tapers from 141 nm to 234 nm. Device simulations via finite-difference-time-domain (FDTD) methods yield a theoretical quality factor of $Q \sim 10,000$, and mode volume of

$$V = 1.8 \left(\frac{\lambda}{n} \right)^3.$$

The relatively large mode volume ensures that the field intensity is strong even at a large distance from the center of the cavity. Figure S1 shows the normalized field intensity inside the diamond along the nanobeam calculated with finite-difference-time-domain (FDTD) method, with the peaks appearing in the dielectric (diamond) region (we suppress the field in the holes in the plot for clarity). As shown in the Figure, there are multiple local maxima for the cavity field. Even at distances as far as 1.3 μm from the global field maximum, we can reach a field intensity $\sim 67\%$ of that at the global field maximum. Therefore, the mode volume of our cavity accommodates a large variation in emitter positioning while preserving relatively strong coupling strength.

Using the SiV density of $3 \times 10^{14} \text{ cm}^{-3}$ from our previous work², we estimate that on average 2.4 emitters per cavity experience $>67\%$ of the maximum field intensity. Therefore, the probabilistic positioning that we rely on is not significantly detrimental compared to the state-of-the-art alternative SiV alignment methods. This is also consistent with our observed device yield where $\sim 50\%$ of the systems contain spectrally stable SiV centers with strong cavity enhancement.

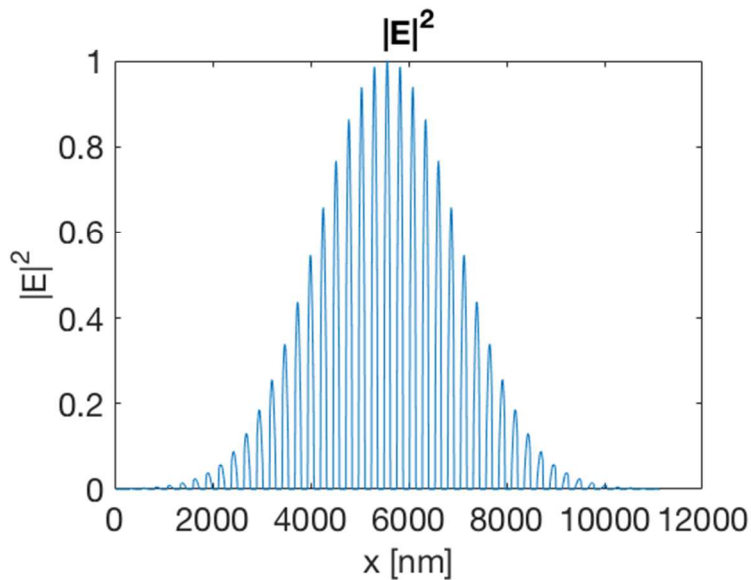


Figure S1: Normalized field intensity as a function of position along the nanobeam. The line cut is taken through the field maximum point in the cavity. Here we have suppressed the field in the hole regions since the emitters can only exist in the dielectric material.

Optical Measurement Set-up

The enhancement of the spontaneous emission rate from the SiV^- center was observed in a confocal microscope set-up in a closed-cycle cryostat at $\sim 4\text{K}$ (Montana Instruments Cryostation). The cavities were excited with a continuous wave (CW) Ti:sapphire laser at 720 nm through a high numerical aperture objective ($\text{NA} = 0.9$), and the photoluminescence is collected through the same objective. The spectrally filtered photoluminescence in the 730-763 nm spectral window was sent either to a high-resolution spectrometer for spectral characterization, or to a streak camera (Hamamatsu C5680) or single photon counting module (SPCM) for the time resolved photoluminescence measurement.

Time-resolved photoluminescence measurements were performed by exciting the SiV^- using 710 nm picosecond pulsed Ti:sapphire laser. In the detuned case, the luminescence from transition B was filtered through a monochromator (Princeton Instruments Acton SP2750), detected by an SPCM, and then the temporal profile was constructed by a Time-Correlated Single Photon Counting (TCSPC) system triggered by the excitation pulses. In the resonant case, the cavity was tuned into resonance with the individual optical transitions by gas condensation, and the spectrally filtered PL emission in the 733-746 nm spectral region was sent to the streak camera for construction of a time-resolved spectrograph.

The optical mode of the nanobeam photonic crystal is red-shifted by injecting argon gas into the cryostat through a precision mass flow controller. The argon condenses onto the cold

surfaces in the cryostat, thereby changing the effective refractive index of the nanobeam photonic crystal cavity and red-shifting the cavity mode. As the cavity is continuously tuned across the four transitions of the SiV^- center, the emission intensities of the individual dipole transitions are strongly enhanced due to coupling to the optical resonator.

Minimum Purcell factor F_{\min}

The Purcell factor for the system measured in Figure 3 is given by^{7,8}

$$F = (\tau_{\text{off}} / \tau_{\text{on}} - 1) / \xi, \quad (1)$$

where $\xi = \frac{\gamma_B}{\gamma_B + \gamma_{\text{rad,other}} + \gamma_{\text{nr}}}$ is the off-resonance branching ratio into transition B. Here γ_B ,

$\gamma_{\text{rad,other}}$, and γ_{nr} are the off-resonance emission rate through transition B, the emission rate through other radiative channels including the phonon sideband, and the non-radiative decay rate, respectively. Here we assume that $\tau_{\text{bulk}} = \tau_{\text{off}}$ in our calculation, where τ_{bulk} is the lifetime in bulk, which agrees with our previous measurements. We do not expect the off-resonant density of states to be significantly modified in the nanobeam photonic crystal since one dimensional photonic crystal suppresses the density of states only one dimension (similar to DBR micropost cavities where the same assumption is made⁹). Experimentally, we did not find strong modification of the density of states beyond emitter to emitter variation, with $\tau_{\text{bulk}} = 1.74 \pm 0.01$ ns. Through quasi-resonant pumping and detection (see next Section), an upper bound for the off-resonance branching ratio of $\xi_{\text{max}} = 0.325$ is extracted. Note that in our calculation for the upper bound branching ratio, we do not include decay into the phonon sideband and non-

radiative transitions. The upper bound branching ratio of $\xi_{\max} = 0.325$ gives a lower bound on the Purcell factor of $F_{\min} = 26.1 \pm 1.8$ according to Equation (1).

Measurement of ξ_{\max}

We employ a quasi-resonant pumping and detection scheme to directly measure the $\xi_{\max} = \gamma_B / (\gamma_B + \gamma_{ACD})$. By quasi-resonantly pumping transition A or B, we ensure that all the emitter dynamics are excited through the upper excited state without direct population of the lower excited state. We resonantly excite transition A (B), as shown by the grey area in Figure S2, and collect the emission from transitions B, C, and D (A, C, and D) on a CCD camera, filtered through an etalon filter (Light Machinery) and a custom-built double monochromator to suppress the excitation laser. Photon emission into orthogonal polarizations is collected (not shown) to obtain the total emission intensity, as shown by the red, black and blue curves in Figure S2. Finally, we combine the results from resonantly driving transitions A and B to obtain the relative emission intensity of all four zero-phonon lines. The percentage of zero-phonon line emission into transitions A, B, C, D are 3.1%, 32.5%, 45.2%, and 19.3%, respectively.

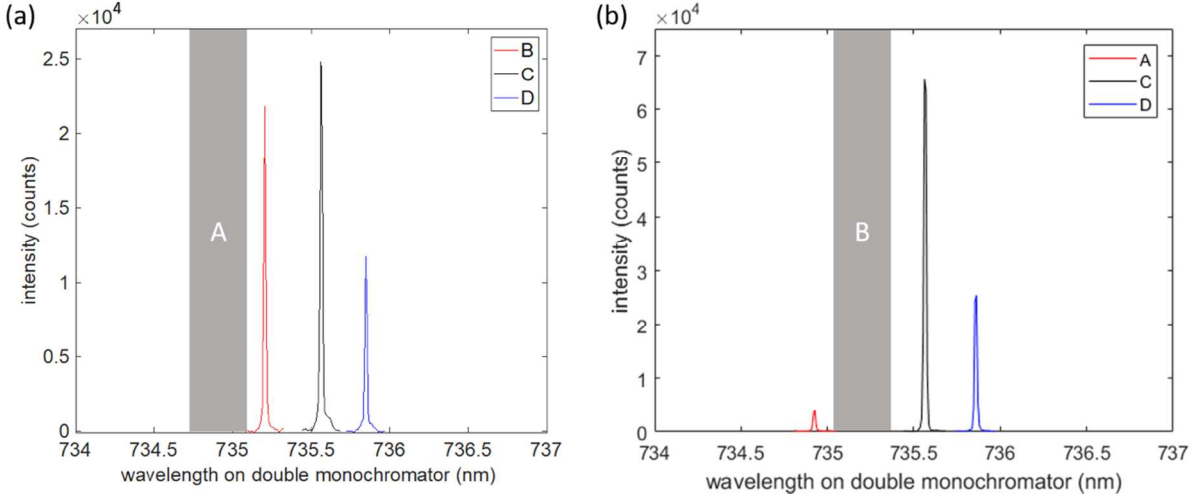


Figure S2: Relative intensities of the zero-phonon line emission under quasi-resonant excitation of transitions A (a) and B (b). The grey areas denote the wavelength of the excitation laser which was filtered with an etalon and a double monochromator.

Comparison to the Theoretical Purcell factor

We calculate the theoretical Purcell factor $F_{theory} = \frac{3}{4\pi^2} \left(\frac{\lambda}{n}\right)^3 \frac{Q}{V}$ using the measured quality factor Q and the simulated mode volume $V = 1.8 \left(\frac{\lambda}{n}\right)^3$, as shown in Table S1. For the representative device described in the main text, the estimated F_{min} is ~ 10.4 times smaller than F_{theory} . Physically, misalignment of the dipole moment from the cavity field orientation and displacement of the emitter from the field maximum reduce the Purcell factor from the theoretically predicted value by a factor of 1/3 and an unknown amount, respectively. In addition, we underestimate F_{min} by using the upper bound value for the branching ratio, which does not account for decay channels through the phonon sideband (30% of radiative emission)

and non-radiative processes. Our analysis is consistent with the estimated upper limit on F for similar cavities in prior works¹⁰.

Table S1: Purcell enhancement of the SiV⁻ centers

SiV ⁻ #	τ_{on} [ns]	τ_{off} [ns]	β (%)	F_{min}	F_{theory}
1	0.340±0.017	1.88±0.02	82.4±1.0	11.1±0.8	350
2	0.208±0.011	1.79±0.02	88.6±0.7	9.4±0.7	282
3	0.194±0.008	1.84±0.04	89.7±0.6	26.1±1.8	272
4	0.158±0.003	1.70±0.02	91.0±0.3	12.6±0.4	262

Analysis of non-radiative decay and its impact on β -factor

To quantitatively analyze the non-radiative decay rate of SiV and its impact on the beta factor, we measure the fraction of emission through transition B. Figure S3 shows the PL spectra when the cavity was resonant with (blue) and far detuned (green) from transition B respectively. While the emission intensity of the resonant transition B is enhanced by a factor of ~ 42 , those of transitions A/C/D are suppressed by factors of 0.44/0.60/0.79, respectively. By binning the emission intensity of each ZPL transition, we find that 95% of all ZPL emission is through the resonant transition B, which is consistent with a calculated β -factor of 89.7±0.6%. We attribute the difference to decay channels through the phonon sideband emission and non-radiative processes. Assuming that the rates of phonon sideband and non-radiative transitions have not been changed by the cavity mode, we can self-consistently calculate a quantum efficiency of at

least 51% for the system. Using $\frac{\gamma_{B,on}}{\gamma_{B,on} + \gamma_{ACD,on}} = 0.95$, $\frac{\gamma_{B,on}}{\gamma_{B,on} + \gamma_{ACD,on} + \gamma_{nr+PSB}} = 0.90$, and

$\gamma_{B,on} + \gamma_{ACD,on} + \gamma_{nr+PSB} = \gamma_{on} = 1/\tau_{on}$, we find $\gamma_{nr+PSB} = 0.263$ GHz, $\gamma_{B,on} = 4.5$ GHz,

$\gamma_{ACD,on} = 0.237$ GHz. Assuming that the rates of phonon sideband and non-radiative transitions

are not changed by the cavity, we can get $\gamma_{ABCD,off} = \gamma_{off} - \gamma_{nr+PSB} = 0.269$ GHz, and the quantum

efficiency of the zero-phonon lines is $\frac{\gamma_{ABCD,off}}{\gamma_{off}} = 51\%$.

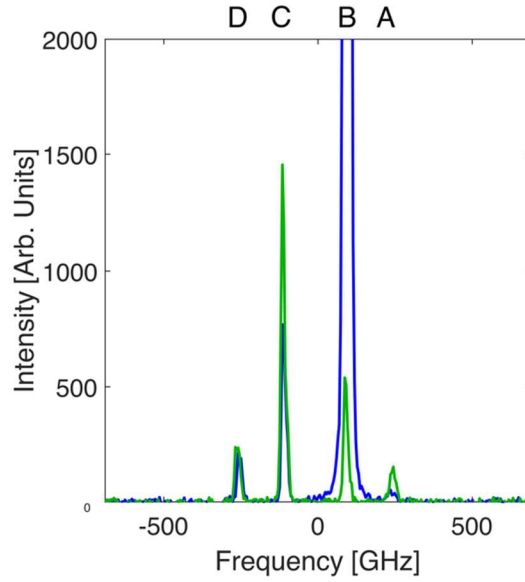


Figure S3: The PL spectra when the cavity is resonant with (blue) and detuned from (green) transition B. The strong PL intensity enhancement of transition B by a factor of 42 leads to suppression of the emission intensities of transitions A/C/D by factors of 0.44/0.60/0.79 respectively. When in resonance with the cavity, 95% of all zero-phonon line emission goes into transition B.

Theoretical model for cavity transmission spectrum

For the bare cavity shown in Figure 4(a) in the main text, the cavity transmission coefficient is given by $t_0 = \frac{\kappa_{ex}/2}{\kappa/2 + i(\omega - \omega_c)}$, where κ is the cavity energy decay rate, κ_{ex} is the cavity

energy decay rate into the waveguide mode, ω is the laser frequency, and ω_c is the cavity frequency. When we couple into the waveguide through the notch at one end, and collect the transmission through the notch at the other end of the waveguide, we might also excite and collect other waveguide or leaky modes that do not couple to the cavity. Thus we numerically fit

the measured cavity spectrum to a function given by $S_{out}(\omega) = A \cdot \left| \frac{\kappa/2}{\kappa/2 + i(\omega - \omega_c)} + qe^{i\alpha} \right|^2 + B$,

where $S_{out}(\omega)$ is the detected intensity of the transmitted laser at frequency ω , A is a scalar that accounts for input laser intensity, collection efficiency, and detection efficiency, B is the collected background counts due to effects such as detector dark noise, and q is a unit-less number that describes the relative amplitude between the modes coupled and uncoupled to the cavity collected by the fiber, and α is the phase between the cavity coupled and uncoupled modes. The free fitting parameters are A , B , q , α , and κ . From the fit to Figure 4(a), we obtain $\kappa/2\pi = 49.7 \pm 2.0$ GHz and $\alpha = (0.97 \pm 0.01)\pi$.

For the dipole induced transparency spectrum, the cavity transmission coefficient is given by

$t = \frac{\kappa_{ex}/2}{\kappa/2 + i(\omega - \omega_c) + 2g_B^2/i(\omega - \omega_B)\gamma_B}$, where g_B is the coupling strength between transition B

and the cavity, and γ_B is the linewidth of transition B when it is far detuned from the cavity. We denote P as the occupation probability of the SiV⁻ in the upper ground states (which couples to the cavity through transition B). The cavity transmission spectrum shown in Figure 4(b) of the

main text is thus given by

$$S_{out}(\omega) = A \cdot \left[(1-P) \left| \frac{\kappa/2}{\kappa/2 + i(\omega - \omega_c)} + qe^{i\alpha} \right|^2 + P \left| \frac{\kappa/2}{\kappa/2 + i(\omega - \omega_c) + 4g_B^2/i(\omega - \omega_B)\gamma_B} + qe^{i\alpha} \right|^2 \right] + B.$$

In the numerical fitting, we fixed A , B , q , α , and κ using the values we obtained in Fig. 4a. We also fixed the parameter γ_B to be $\gamma/2\pi = 1.36$ GHz obtained through photoluminescence excitation measurements when it is far detuned from the cavity. The only free fitting parameters are P and g_B .

To accurately obtain P and g_B together, we also measure the cavity transmission spectrum when the cavity is resonant with transition C. The blue circles in Figure S4 shows the measured data. In this case, the cavity transmission spectrum is given by

$$S_{out}(\omega) = A \cdot \left[P \left| \frac{\kappa/2}{\kappa/2 + i(\omega - \omega_c)} + qe^{i\alpha} \right|^2 + (1-P) \left| \frac{\kappa/2}{\kappa/2 + i(\omega - \omega_c) + 4g_C^2/i(\omega - \omega_B)\gamma_C} + qe^{i\alpha} \right|^2 \right] + B,$$

where g_C is the coupling strength between transition C and the cavity, and γ_C is the linewidth of transition C when it is far detuned from the cavity. Note that the probability that the SiV⁻ modifies the cavity spectrum is now given by $1-P$. We fit both the data in Fig. 4(b) and Figure S4 using the same set of fitting parameters. We obtain that $P = 0.24 \pm 0.02$, $g_B/2\pi = 4.9 \pm 0.3$ GHz, and $g_C/2\pi = 1.4 \pm 0.1$ GHz. We attribute the difference in the coupling strength for transitions B and C to strain induced polarization distortion between the selection rule of the two transitions.

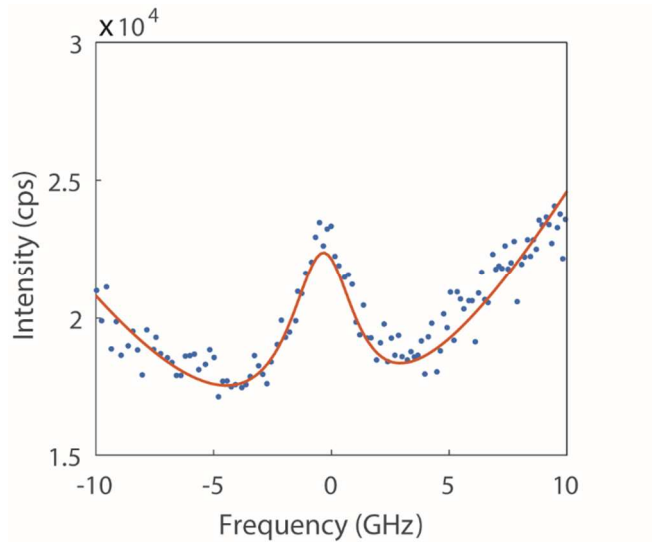


Figure S4: Cavity transmission spectrum when the cavity is resonant with transition C. Blue circles show measured data, and red solid line shows numerical fit to the model.

References:

1. Zhang, J. L.; Ishiwata, H.; Babinec, T. M.; Radulaski, M.; Muller, K.; Lagoudakis, K. G.; Dory, C.; Dahl, J.; Edgington, R.; Souliere, V.; Ferro, G.; Fokin, A. A.; Schreiner, P. R.; Shen, Z. X.; Melosh, N. A.; Vuckovic, J., *Nano Lett* **2016**, *16* (1), 212-7.
2. Zhang, J. L.; Lagoudakis, K. G.; Tzeng, Y.-K.; Dory, C.; Radulaski, M.; Kelaita, Y.; Fischer, K. A.; Shen, Z.-X.; Melosh, N. A.; Chu, S.; Vučković, J., **2017**, *arXiv:1701.04961*.
3. Burek, M. J.; Meuwly, C.; Evans, R. E.; Bhaskar, M. K.; Sipahigil, A.; Meesala, S.; Sukachev, D. D.; Nguyen, C. T.; Pacheco, J. L.; Bielejec, E., **2016**, *arXiv:1612.05285*.
4. Latawiec, P.; Burek, M. J.; Sohn, Y.-I.; Lončar, M., *Journal of Vacuum Science & Technology B, Nanotechnology and Microelectronics: Materials, Processing, Measurement, and Phenomena* **2016**, *34* (4), 041801.
5. Burek, M. J.; de Leon, N. P.; Shields, B. J.; Hausmann, B. J.; Chu, Y.; Quan, Q.; Zibrov, A. S.; Park, H.; Lukin, M. D.; Loncar, M., *Nano Lett* **2012**, *12* (12), 6084-9.
6. Burek, M. J.; Chu, Y.; Liddy, M. S.; Patel, P.; Rochman, J.; Meesala, S.; Hong, W.; Quan, Q.; Lukin, M. D.; Loncar, M., *Nat Commun* **2014**, *5*, 5718.
7. Faraon, A.; Barclay, P. E.; Santori, C.; Fu, K.-M. C.; Beausoleil, R. G., *Nature Photonics* **2011**, *5* (5), 301-305.
8. Faraon, A.; Santori, C.; Huang, Z.; Acosta, V. M.; Beausoleil, R. G., *Phys Rev Lett* **2012**, *109* (3), 033604.
9. Vučković, J.; Fattal, D.; Santori, C.; Solomon, G. S.; Yamamoto, Y., *Applied Physics Letters* **2003**, *82* (21), 3596-3598.

10. Sipahigil, A.; Evans, R. E.; Sukachev, D. D.; Burek, M. J.; Borregaard, J.; Bhaskar, M. K.; Nguyen, C. T.; Pacheco, J. L.; Atikian, H. A.; Meuwly, C.; Camacho, R. M.; Jelezko, F.; Bielejec, E.; Park, H.; Loncar, M.; Lukin, M. D., *Science* **2016**, 354 (6314), 847-850.